ADVANCED ENERGY & SUSTAINABILITY RESEARCH
Open Access
www.advenergysustres.com

Phase Evolution and Li Diffusion in LATP Solid-State Electrolyte Synthesized via a Direct Heat-Cycling Method

Thomas E. Ashton, Peter J. Baker, Yiana S. Shakespeare, Daniel Commandeur, and Jawwad A. Darr*

Herein, the direct synthesis of phase-pure lithium aluminum titanium phosphate ($Li_{1.3}Al_{0.3}Ti_{1.7}(PO_4)_3$, LATP) solid-electrolyte powder in 220 min and relatively low temperatures (850 °C) is achieved via a new (cyclic) fast heat treatment (c-FHT) route. The complex structural evolution highlights rate-limited lithium incorporation of intermediate metal phosphates formed prior to the final phase-pure LATP. The prepared LATP product powder displays similar bulk (2×10^{-10} cm^2 s^{-1}) and local (3×10^{-10} cm^2 s^{-1}) values for lithium diffusion coefficients (D_{Li}) characterized by electrochemical impedance spectroscopy and muon spin relaxation (μSR), respectively. The similarity between both D_{Li} values suggests excellent retention of inter- and intraparticle lithium diffusion, which is attributed to the absence of deleterious surface impurities such as $AlPO_4$. A low-energy barrier ($E_a = 73$ meV) of lithium diffusion is also estimated from the μSR data.

1. Introduction

Lithium-ion batteries (LIBs) remain the most competitive energy storage solution for global electrification and automotive applications.[1] However, several key challenges still remain to improve their performance in high-power applications. Conventional LIBs rely on the use of lithium salts dissolved organic liquid electrolytes, such as $LiPF_6$ in a mixture of ethylene carbonate and dimethyl carbonate.[2] Whilst generally successful, these conventional electrolytes have repeatedly come under scrutiny due to their flammability risks and limit on maximum achievable cell voltages.[3,4] This is due to electrolyte degradation, especially when used in conjunction with a high-capacity lithium metal anode.[3] One solution has been a move toward an all solid-state battery (SSB), swapping organic-based electrolytes for an inorganic solid-state electrolyte (SSE).[5]

Currently, garnet-type SSEs, particularly $Li_7La_3Zr_2M_xO_{12}$ (LLZO; M = Ta, Nb, Ga etc.), dominate the research arena with continued and extensive studies.[6,7] Although these materials have shown great promise for use in SSBs with a lithium metal anode, there is still concern over the following: 1) instability in contact with moisture, causing formation of inactive $LiCO_3$; 2) cost and availability of rare earth dopants; 3) difficulty in manufacturing artifacts due to large energy barriers for sintering and subsequent Li vaporization/phase transformation.[8–11]

Lithium conducting glass ceramics (LCGCs), such as lithium aluminum titanium phosphate ($Li_{1.3}Al_{0.3}Ti_{1.7}(PO_4)_3$, LATP), present a potential solution to the challenges encountered with garnet-structured SSEs.[12] LATP comprises relatively cheap substituent metal elements (Al and Ti) compared to those found in LLZO, specifically the rare earth dopants (Ta, Nb, Ga). LCGCs have also shown excellent resistance to moisture making them ideal for applications in Li–air batteries.[13] Furthermore, their glass nature allows melts to be formed, and artifacts can be manufactured using well-established industrial casting processes, similar to optical glasses.[14] However, LATP powders are usually produced as a convenient intermediary prior to final artifact sintering and processing, or to use in emerging organic–inorganic composite electrolytes.[15,16] Typically, these powders are produced by solid-state heat treatments of metal oxide precursors over long durations (≥12 h) at elevated temperatures (≥900 °C).[14] Alternative approaches, such as urea–flux-mediated heat treatments, have been reported, but also require long durations (≥7 h) consisting of multiple steps at elevated temperatures.[17] Solid-state syntheses are also hampered by the prevalence of $AlPO_4$ impurities, typically found at grain boundaries, that significantly reduce ionic conductivity and ultimately limit electrochemical performance.[18] Rapid LATP synthesis techniques have also been explored such as spark plasma sintering (SPS), field-assisted synthesis technique (FAST), and ultrafast high-temperature sintering (UHS).[19–21] However, SPS and FAST are both energy intensive and all three are best suited to dense artifact formation rather than powder synthesis. Thus, challenges still remain in reducing times and temperatures to drive down manufacturing costs and complement existing techniques.

T. E. Ashton, Y. S. Shakespeare, D. Commandeur, J. A. Darr
Department of Chemistry
University College London
Bloomsbury WC1H 0AJ, London, UK
E-mail: t.ashton@ucl.ac.uk

P. J. Baker
ISIS Pulsed Neutron and Muon Source
STFC Rutherford Appleton Laboratory
Didcot OX11 0QX, Oxfordshire, UK

The ORCID identification number(s) for the author(s) of this article can be found under https://doi.org/10.1002/aesr.202200017.

DOI: 10.1002/aesr.202200017

Additionally, fully understanding the electrochemical behavior and fundamental mechanics that underpin performance is a continuing challenge in LIB materials. The diffusion of lithium in SSEs ultimately dominates their performance in an electrochemical cell, thus its study is crucial to SSE and SSB materials development.[22] Many techniques are available to study diffusion within battery materials such as LATP, including electrochemical techniques,[23] solid-state nuclear magnetic resonance (NMR),[24] and computational methods.[25] Each of these have their own associated experimental caveats: electrochemical impedance spectroscopy (EIS), galvanostatic intermittent titration techniques (GITTs), and cyclic voltammetry (CV) are bulk electrochemical techniques sensitive to the experiment geometry, cell chemistry, and materials' micro-/mesostructure; solid-state NMR spectroscopy is limited by magnetic elements in the sample; computational atomistic methods focus on idealized structures. Each of these may be viewed as advantages or disadvantages, depending on the experimental question.

μSR has been rapidly developing as a cutting-edge technique, allowing intimate insight into the diffusion mechanics of ionic conductors.[26] In contrast to other related techniques, muons are used as local probes to investigate the diffusion on an atomic scale, independent of bulk influences. Thus, μSR becomes a powerful tool in combination with bulk electrochemical techniques to separate the local and bulk influences on diffusion, and inform materials design and development. Herein, we investigate the use of a novel cyclic fast heat treatment (c-FHT) to characterize the phase evolution and access single-phase LATP in relatively short times. For the first time, we present experimental data investigating the phase evolution during synthesis and the local diffusion mechanics in LATP.

2. Results and Discussion

2.1. Structural Characterization

To investigate the structural evolution of LATP, solid-state c-FHT was carried out in an open tube furnace at 850 °C. Briefly, the oxide precursor mixture was placed into the preheated furnace for 20 min and subsequently removed, cooled down to room temperature and ground in an agate mortar. The flash heating process was repeated a further 1–10 times, up to a cumulative heat treatment duration of 220 min. The resulting 11 white powders were analyzed using powder X-Ray diffraction (PXRD), shown in **Figure 1**a. After 20 min of heat treatment (one cycle), the sample displayed broad diffraction peaks corresponding to rutile TiO_2 (space group: $P4_2/mnm$). Increasing the heat-treatment duration led to dramatic peak narrowing, suggesting an increase in crystallinity commensurate with solid-state preparation. From 40 to 200 min (two to ten cycles), three coexistent crystalline phases were identified: 1) a $Pa\bar{3}$-structured titanium pyrophosphate (TiP_2O_7), 2) a $C222_1$-structured $AlPO_4$, and 3) a $R\bar{3}c$ phase typical of LATP.[27] No Li-containing impurities were identified, likely due to low Z of Li (and thus weak interaction with laboratory X-Ray radiation) or its presence as amorphous material. To understand the evolution of these phases in greater detail, multiphase Rietveld refinement was conducted on each sample using standard patterns for TiP_2O_7, $AlPO_4$, and LATP (ICSD Coll. Code: 189 807, 97 546, and 14 585, respectively). The estimated phase ratios at each cumulative duration are given in Figure 1b.

Overall, increasing the heat-treatment duration led to a sigmoidal growth in the LATP phase percentage, and sigmoidal decline in TiP_2O_7 and $AlPO_4$. At 40 min (two cycles), the major phase (≈64%) was TiP_2O_7, with only 24% of the desired LATP crystal phase and 12% $AlPO_4$. Beyond a cumulative heat-treatment time of 120 min (six cycles), the $R\bar{3}c$ LATP structure became dominant and the TiP_2O_7 and $AlPO_4$ impurities continued to decrease with time. Ultimately, at 220 min (eleven cycles), a phase-pure LATP sample was obtained with contributions from TiP_2O_7 and $AlPO_4$ below the limit of detection. The Rietveld profile for the pure material is given in **Figure 2**a (structural parameters are given in Table S1, Supporting Information), showing excellent agreement with a NaSICON-type $R\bar{3}c$-structured $Li_{1.3}Al_{0.2}Ti_{1.8}(PO_4)_3$ and no observable impurity phases ($\chi^2 = 2.06$). The differences in residual intensity of the observed and calculated diffraction pattern are due to instrumental asymmetry (transmission geometry). These observations suggest that the rate limiting factor in the preparation of phase-pure LATP at this temperature is the reaction of the Li source with the intermediate metal phosphates. However, the c-FHT methodology provided phase-pure LATP powders more rapidly than conventional heat treatments for LATP powders that are typically on the order of 8–12 h of continuous heating.[14]

Figure 2b shows the Raman spectrum collected for the 220 min (eleven 20 min cycles) LATP sample. Several features were identified, consistent with previous reports: 1) P–O stretching at 850–1130 cm^{-1}; 2) P–O bending at 400–680 cm^{-1}; 3) Ti^{4+} and PO_4^{3-} transitional vibrations, and PO_4^{3-} librations at 200–400.[28,29] Preceding studies have noted that the three spectral peaks labeled A (969 cm^{-1}), B (989 cm^{-1}), and C (1007 cm^{-1}) broaden with increasing substitution of Al or Li with Ti.[30,31] Qualitatively, the spectrum for LATP herein compares most closely to a partially substituted sample, $Li_{1.3}Al_{0.2}Ti_{1.8}(PO_4)_3$, in good agreement with the Rietveld refinement. Notably, no discernible contributions from potential impurity phases, including $AlPO_4$, TiP_2O_7, $LiCO_3$, TiO_2, Al_2O_3, or $Li_2Ti_xO_y$, were identified.

Scanning electron microscopy (SEM) was used to investigate the microstructure of the LATP sample, showing unremarkable secondary agglomerates ($\varnothing = 10$–70 μm) of smaller primary particles ($\varnothing = 100$–800 nm) typical of solid-state synthesis (Figure S1, Supporting Information).[14]

2.2. Electrochemical Impedance Spectroscopy

The bulk diffusion of the phase-pure LATP sample was investigated by EIS. The Nyquist plot is shown in **Figure 3**, with two typical components: 1) a semicircle at low frequency representing the bulk impedance of the LATP and 2) a ≈45° tail at low frequency attributed to the Warburg impedance (semi-infinite linear diffusion) from diffusion of Li.[32] D_{Li} was calculated using Equation (1) where R is the gas constant, T is the experimental temperature, A is the surface area of the electrode, F is the Faraday constant, σ_w is the Warburg coefficient, and C is the molar concentration of Li^+ ions.

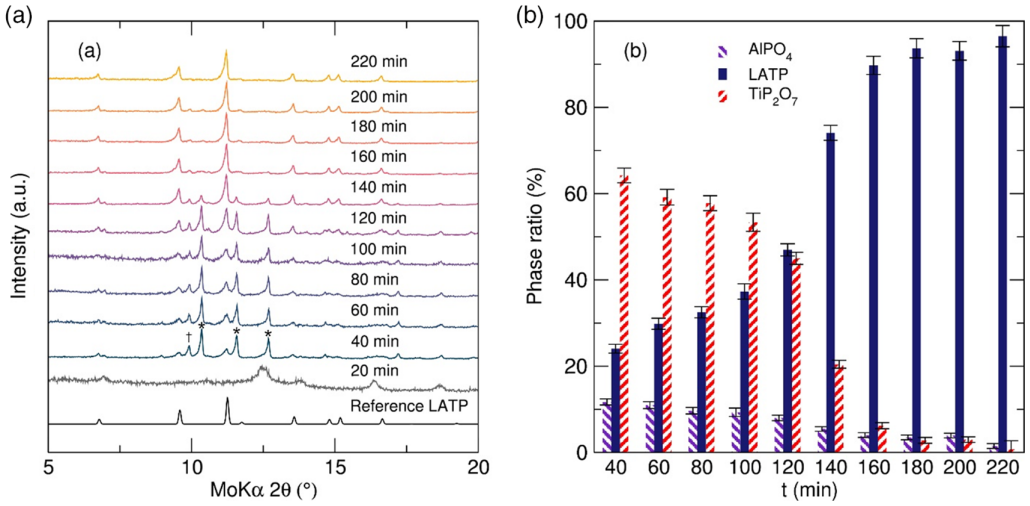

Figure 1. a) Powder X-Ray diffraction patterns during the attempted synthesis of $Li_{1.3}Al_{0.3}Ti_{1.7}(PO_4)_3$ (LATP) at increasing heat-treatment duration showing mixtures of $Pa\bar{3}$ TiP_2O_7 (*), $C222_1$ $AlPO_4$ (†), and $R\bar{3}c$ LATP. b) Phase ratios estimated by multiphase Rietveld refinement at each temperature using reference patterns for TiP_2O_7, $AlPO_4$, and LATP (ICSD Coll. Code: 189807, 97546, and 14585, respectively).

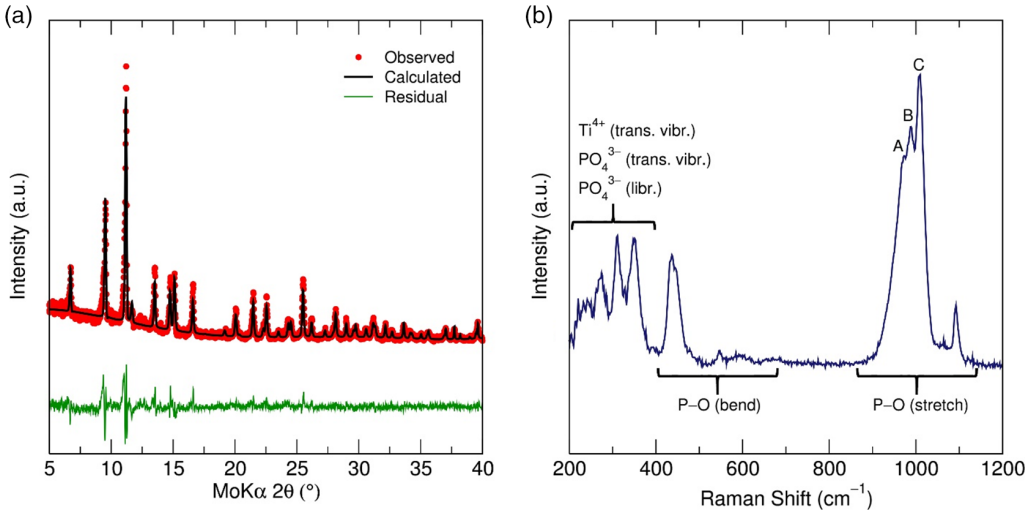

Figure 2. a) Rietveld refinement of LATP prepared after 220 min of heat-treatment at 850 °C showing a good agreement to single-phase $R\bar{3}c$ structure (ICSD Coll. Code: 14585). b) Raman spectrum of LATP.

$$D_{Li} = 0.5\left(\frac{RT}{AF^2\sigma_w C}\right)^2 \quad (1)$$

σ_w is calculated from the slope of Z_{re} versus the reciprocal square root of the angular frequency ($\omega^{-0.5}$) over the Warburg range. The value of σ_w estimated by fitting the data to an equivalent circuit (Figure 3 inset). Other relevant values for the fit are given in Table S2, Supporting Information. The bulk diffusion coefficient from EIS was calculated to be 2.24^{-10} cm^2 s^{-1}.

2.3. Muon Spin Relaxation

To intimately understand the local diffusion within the LATP sample, muon spin relaxation (μSR) was performed. **Figure 4**a shows the raw data collected at 300 K with three separately applied longitudinal magnetic fields (B_{LF}) of 0 (zero field), 5 and 10 G to decouple the muon relaxation from nuclear magnetic fields within the sample. As magnetic flux density increased, a corresponding decrease in the relaxation of the muon decay asymmetry was observed due to this decoupling. The relaxation behavior is typical of diffusion mediated perturbation of muon spin polarization from ^{6}Li and ^{7}Li.[33] Data collected at three fields from 100 to 500 K in 20 K intervals were subsequently fit using Equation (2).[34] $A_F \exp(-\lambda_F t)$ is an exponentially relaxing component that describes the contribution from nuclear magnetic spins on the muon relaxation. $A_{KT} \exp(-\lambda_{KT} t) \times G^{DGKT}(\Delta, \nu, t, H_{LF})$ is a modified Kubo–Toyabe (KT) relaxation model describing the dynamic diffusion processes multiplied

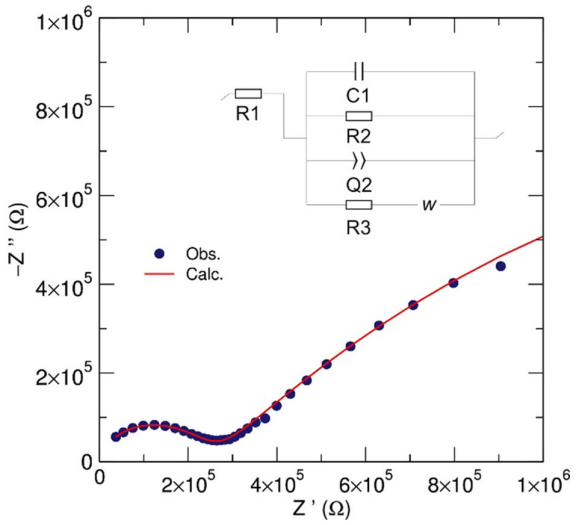

Figure 3. Nyquist plot for the electrochemical impedance spectroscopy conducted on LATP with the equivalent circuit used to model the data (inset).

by a Gaussian relaxation function to account for temperature independent fluctuations in Li^+ diffusion. A_{BG} is a constant background component.

$$A_0 P_{LF}(t) = A_F \exp(-\lambda_F t) + A_{KT} \exp(-\lambda_{KT} t) \times G^{DGKT}(\Delta, \nu, t, H_{LF}) + A_{BG} \quad (2)$$

As lithium ions diffuse through the LATP structure, they perturb the decay of nearby muons implanted in the sample. The rate of these perturbations, known as the fluctuation rate (ν), is thus directly proportional to the rate of lithium diffusion (D_{Li}). Figure 4b shows the values of ν extracted using the KT model. Thermal activation of Li^+ diffusion was observed from 200 to 380 K, characterized by an exponential increase in ν. Above 380 K, the Li diffusion in LATP became too rapid to be monitored by μSR and ν began to decrease. Figure 4c shows the field distribution width (Δ) for each temperature. A slow decrease was observed from 200 to 500 K due to the motional narrowing of the magnetic environment the muon experienced, commensurate with preceding studies.[33,35,36] D_{Li} was estimated by employing Equation (3).

$$D_{Li} = \sum_{i=1}^{n} \frac{1}{N_i} Z_{\nu,i} s_i^2 \nu \quad (3)$$

where N_i is the number of accessible Li^+ sites in the ith path, $Z_{\nu,i}$ is the vacancy fraction of the destination sites, s_i is the jump distance between Li^+ sites, and ν is the fluctuation rate at a given temperature.[37] **Figure 5** shows the electron density map for the *hkl* (0 1–4) plane along which diffusion occurs in LATP through three steps: 1) fully occupied M1 (*6b*) to partially occupied M3 (*36f*), M1→M3; 2) partially occupied M3 (*36f*) to partially occupied M3 (*36f*), M3→M3; and 3) partially occupied M3 (*36f*) to fully occupied M1 (*6b*) M3→M1. Ultimately, these pathways culminate in an M1→M3→M3→M1 (*6b*→*36f*→*36f*→*6b*) diffusion chain, previously established by structural and computational studies.[25] Due to the significantly lower occupancy of Li on the M3 site (5%), the fully occupied M1 dominates the contribution to diffusion at room temperature. The distance between these sites in the LATP sample was extracted from the Rietveld refinement (Table S1, Supporting Information), leading to a diffusion coefficient (D_{Li}) of 2.77×10^{-10} $cm^2 s^{-1}$ at 300 K, in excellent agreement with the EIS analysis. **Figure 6**a shows the values of D_{Li} from 200 to 400 K, showing a consistent increase commensurate with fundamental thermodynamic principles. A rearrangement of the Nernst–Einstein equation Equation (4)) was used where necessary to convert between conductivity ($S cm^{-1}$) and diffusivity ($cm^2 s^{-1}$), where Λ is the conductivity, z_i is the charge of the diffusing species (Li = 1), F is the Faraday constant, R is the gas constant and T is the experimental temperature.

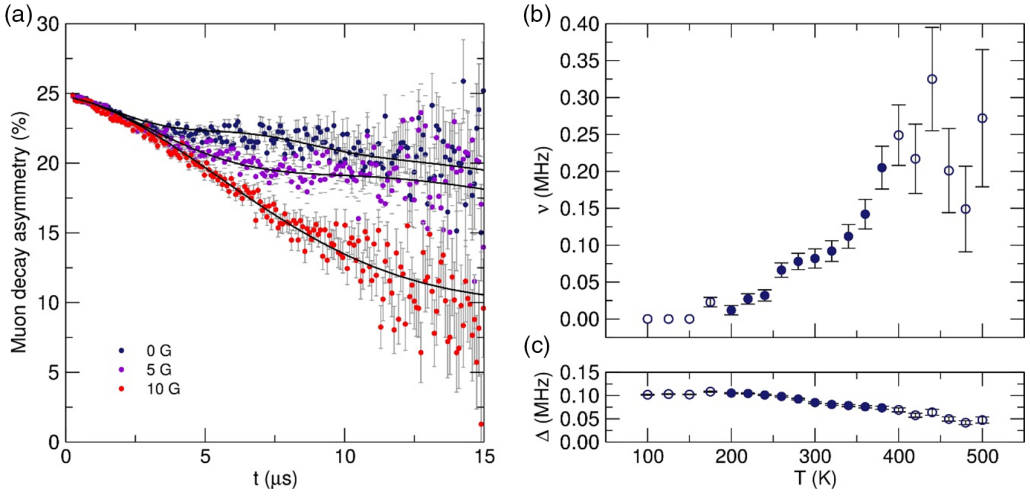

Figure 4. a) Raw data muon spin relaxation data collected at 300 K and modified Kubo–Toyabe fit for LATP with applied longitudinal magnetic fields of 0, 5, and 10 G. b) Fluctuation rate, ν, and c) field-distribution width, Δ, values extracted from fitting the raw LATP muon data.

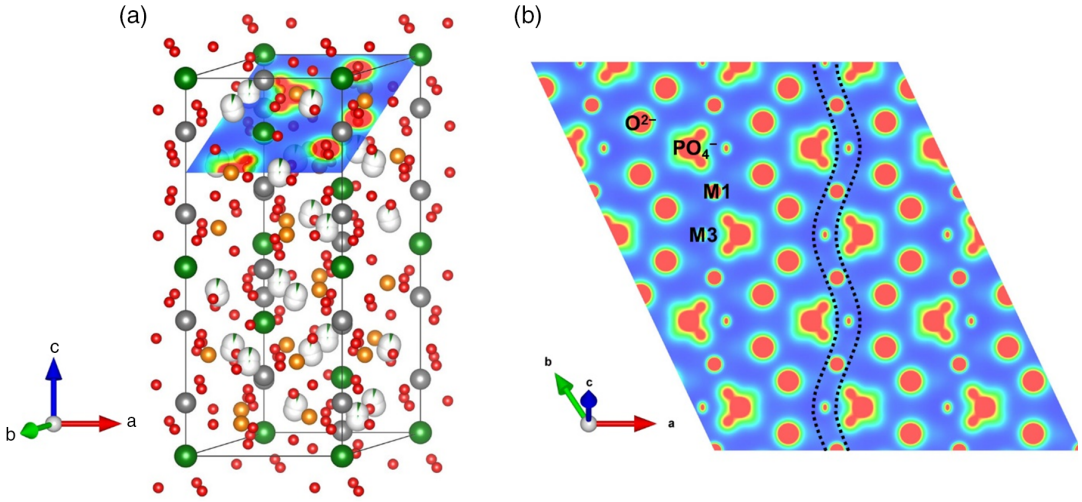

Figure 5. a) Single unit cell of LATP showing positions of oxygen (red), Ti/Al (grey), phosphorous (orange) and lithium (green). b) The electron density map along the (0.1−4) diffusion plane generated from Rietveld refinement, with the M1→M3→M3→M1 diffusion pathway highlighted between dashed lines.

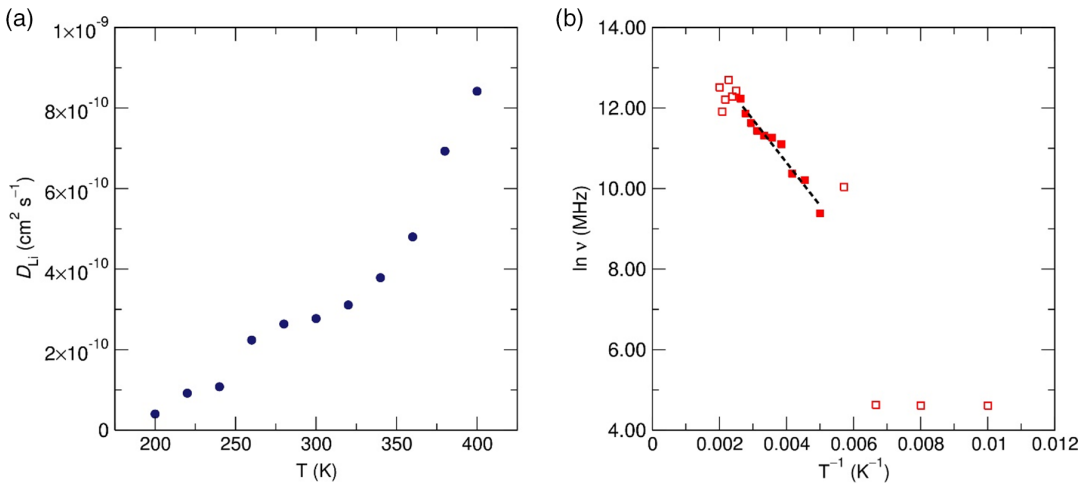

Figure 6. a) Estimated values of D_{Li} for cyclic fast heat treatment (c-FHT) LATP using muon spin relaxation versus temperature. b) Arrhenius plot of the fluctuation rate and linear regression (dashed line) over the thermally activated region (solid squares) for lithium diffusion.

$$\Lambda = \frac{z_i^2 F^2}{RT} D \therefore D = \frac{RT}{z_i^2 F^2} \Lambda \tag{4}$$

The tabulated values of D_{Li} are given in **Table 1**, showing a generally good agreement with the values for several compositions of elemental LATP from the literature. However, μSR suggests a lower value for D_{Li} ($\approx 10^{-10}$ cm^2 s) compared to the values extracted from EIS ($\approx 10^{-9}$ cm^2 s^{-1}) for the specific composition of $Li_{1.3}Al_{0.3}Ti_{1.7}(PO_4)_3$.

Figure 6b shows the Arrhenius plot using the values of ν, and the linear regression fit over the thermally active region. The activation energy (E_a) of lithium hopping was estimated from the slope of the linear regression, giving a value of ≈73 meV. Compared to the literature (Table 1), the value of E_a is significantly lower than EIS. This is a common observation with local μSR studies; EIS is a bulk analysis technique and as such the D_{Li} may be heavily influenced by interparticle diffusion across grain boundaries. As a result, the particle microstructure is particularly important for EIS measurements. Previous reports have found that $AlPO_4$ impurities may present themselves on the surface of LATP particles, lowering the interparticle diffusion of Li. From our studies, no $AlPO_4$ impurities were found in the phase-pure LATP and the bulk diffusion measured by EIS and local diffusion measured by μSR presented similar values of D_{Li}. Thus, the c-FHT synthetic approach may also improve diffusion by limiting deleterious impurities at the interparticle diffusion interface.

3. Conclusions

Phase-pure LATP powder was successfully synthesized by a c-FHT methodology after eleven cycles of 20 min heat treatments at 850 °C. The cumulative time (220 min) was overall shorter in duration than conventional solid-state heat-treatment routes

Table 1. Tabulated values of the ionic conductivity, diffusion coefficient, and activation energy estimated from μSR versus values from the literature. The Nernst–Einstein equation was employed to convert from S cm^{-1} to cm^2 s^{-1} where necessary.

Formula	σ_{Li} [S cm^{-1}]	D_{Li} [cm^2 s^{-1}]	E_a [meV]	Technique	T [K]	References
$Li_{1.3}Al_{0.3}Ti_{1.7}(PO_4)_3$	8×10^{-4}	3×10^{-10}	73	μSR	300	This study
$Li_{1.3}Al_{0.3}Ti_{1.7}(PO_4)_3$	8×10^{-4}	2×10^{-10}	–	EIS	300	This study
$Li_{1.3}Al_{0.3}Ti_{1.7}(PO_4)_3$	6×10^{-3}	–	330	minimum entropy method (MEM)	–	[25]
$Li_{1.3}Al_{0.3}Ti_{1.7}(PO_4)_3$	8×10^{-3}	2×10^{-9}	300	EIS	RT	[41]
$Li_{1.3}Al_{0.3}Ti_{1.7}(PO_4)_3$	4×10^{-2}	4×10^{-9}	190	EIS	RT	[42]
$Li_{1.4}Al_{0.4}Ti_{1.6}(PO_4)_3$	2×10^{-4}	5×10^{-11}	350	EIS	RT	[43]
$Li_{1.5}Al_{0.5}Ti_{1.5}(PO_4)_3$	4×10^{-3}	1×10^{-9}	300	EIS	RT	[44]
$Li_{1.7}Al_{0.7}Ti_{1.3}(PO_4)_3$	4×10^{-3}	8×10^{-10}	300	EIS	RT	[44]
$Li_{1.3}Al_{0.3}Ti_{1.7}(PO_4)_3$	–	–	147–191	EIS	RT	[45]

(typically ≈12 h), presenting a more energetically economic manufacturing route. In addition, c-FHT can be carried out with simple, abundant oxide starting materials and no excess lithium further lowering production costs. The authors believe that c-FHT complements the toolbox of existing techniques by providing access to LATP powders for use in further rather than solid artifacts produced by SPS, FAST, and UHS. The evolution of structural phases was also monitored after each heat-treatment cycle, suggesting the reaction of the Li source with intermediate metal phosphate phases was the rate-limiting step.

LATP syntheses are commonly carried out in the presence with an excess of the lithium precursor to combat evaporation at elevated temperatures, which is not required for c-FHT. Thus, the choice of 850 °C with no excess lithium appears to be sensible for the experiment as it is possible for the solid-state reactions to happen, whilst limiting lithium evaporation. Furthermore, each flash heat-treatment step allows the formation of intermediate phosphate phases, and upon subsequent heating, sufficient semi-volatile lithium is available to drive toward phase-pure LATP. It is likely that upon further investigations at higher temperatures and shorter times, that it may be possible to achieve the desired product with even greater efficiency.

Excitingly, the phase-pure LATP showed similar values of D_{Li} for both the bulk (2×10^{-10} cm^2 s^{-1}) and local (3×10^{-10} cm^2 s^{-1}) diffusion from EIS and μSR, respectively. These observations suggest good intra- and interparticle diffusion, likely due to limiting the formation of surface impurities (such as $AlPO_4$) that are detrimental to diffusion, through the c-FHT methodology employed herein. Activation energies of lithium diffusion were also estimated by μSR as 73 meV, in good agreement with other studies of SSEs by μSR.

4. Experimental Section

Synthesis of Lithium Aluminum Titanium Phosphate: Lithium aluminum titanium phosphate ($Li_{1.3}Al_{0.3}Ti_{1.7}PO_3$, LATP) was prepared by a cyclic c-FHT. All materials were supplied by Sigma-Aldrich, Dorset, UK. Stoichiometric TiO_2 (<100 nm, > 99.9%), Al_2O_3 (<50 nm, >99.9%), $LiOH{\cdot}H_2O$ (>99.9%), and $(NH_4)H_2PO_4$ (>99.9%) were first ground in a Thinky mixer at 1500 RPM for 30 min using ZrO_2 balls. The resulting mixture was then transferred to an alumina crucible and placed into a preheated tube furnace for 20 min and subsequently rapidly removed and cooled. This was repeated a specific number of times (up to 11 cycles) for each sample. After heating for a specific number of cycles, the crucible was removed, and the resulting powder was ground using an agate pestle and mortar for analysis. No intermediate grinding was carried out between heat-treatment cycles.

Structural Characterization (PXRD): PXRD patterns were collected using an Stoe Stadi P diffractometer (Mo Kα radiation, 0.70932 Å) in transmission geometry equipped with a germanium (111) monochromator and a DECTRIS Mythen 1 k silicon strip detector (DECTRIS, Baden, Switzerland). An Yttria (Y_2O_3) standard was used to estimate instrumental peak broadening. Datasets were collected over the 2θ range of 2°–40° with a step size of 0.5° and a count time of 5 s per step. Graphical structural models and electron density maps were generated using the VESTA software package. Rietveld refinement was used to estimate the phase ratios in each prepared sample using the FullProf package.[38]

Scanning Electron Microscopy: SEM was performed using a JEOL JSM-6700 F microscope. To minimize charging, samples were deposited on copper foil tape, mounted on aluminum stubs, after dispersion in methanol (99.9%, Sigma Aldrich, Dorset, UK) and ultrasonication in a XUBA3 Ultrasonic Bath (Grant Instruments, Cambridge, UK) for 5 min. Image analysis was carried out using ImageJ software.[39]

Electrochemical Impedance Spectroscopy: EIS was carried out on a Biologic VMP3 potentiostat. The powder sample was pressed into a pellet inside a Swagelok cell and analyzed between 0.1 Hz and 100 MHz at 5 mV root mean square (RMS) potential amplitude. The resulting data were fit using the ZFit software and further details are given in the Supporting Information.

Local Diffusion Analyses (μSR): μSR experiments were performed at STFC ISIS Neutron and Muon Source, Didcot, UK. ≈3 g of powdered material (LATP) was packed into recessed titanium samples holders, covered with a titanium window and secured with a titanium bezel. The titanium holder provides a simple background signal from muons, which are not implanted into the sample and is easily subtracted from the data. The sample holder was placed into the muon spectrometer (EMU) and evacuated to $<1 \times 10^{-6}$ mBar. The instrument was cooled to a temperature of 100 K and the instrument asymmetry was measured using a transverse magnetic field of 20 G. Measurements were taken every 20 up to 500 K with applied longitudinal magnetic fields of 0, 5, and 10 G. Data collected at each temperature for the three applied magnetic fields were fit simultaneously using the WiMDA software package.[40]

Supporting Information

Supporting Information is available from the Wiley Online Library or from the author.

Acknowledgements

Muon experiments at the ISIS Neutron and Muon Source were supported by a beamtime allocation RB2090035 from the Science and Technology Facilities Council. The authors would also like to thank the Innovate UK grant 104424, The PowerDrive Line, for support.

Conflict of Interest

The authors declare no conflict of interest.

Data Availability Statement

The data that support the findings of this study are available from the corresponding author upon reasonable request.

Keywords

batteries, diffusion, LATP, Li-ions, solid electrolytes

Received: January 30, 2022
Revised: April 6, 2022
Published online:

[1] S. Koohi-Fayegh, M. A. Rosen, *J. Energy Storage* **2020**, *27*, 101047.
[2] Y. Chen, Y. Kang, Y. Zhao, L. Wang, J. Liu, Y. Li, Z. Liang, X. He, X. Li, N. Tavajohi, B. Li, *J. Energy Chem.* **2021**, *59*, 83.
[3] C. Arbizzani, G. Gabrielli, M. Mastragostino, *J. Power Sources* **2011**, *196*, 4801.
[4] S. Hess, M. Wohlfahrt-Mehrens, M. Wachtler, *J. Electrochem. Soc.* **2015**, *162*, A3084.
[5] Q. Zhao, S. Stalin, C.-Z. Zhao, L. A. Archer, *Nat. Rev. Mater.* **2020**, *5*, 229.
[6] Q. Liu, Z. Geng, C. Han, Y. Fu, S. Li, Y. He, F. Kang, B. Li, *J. Power Sources* **2018**, *389*, 120.
[7] P. M. Gonzalez Puente, S. Song, S. Cao, L. Z. Rannalter, Z. Pan, X. Xiang, Q. Shen, F. Chen, *J. Adv. Ceram.* **2021**, *10*, 933.
[8] A. Sharafi, S. Yu, M. Naguib, M. Lee, C. Ma, H. M. Meyer, J. Nanda, M. Chi, D. J. Siegel, J. Sakamoto, *J. Mater. Chem. A* **2017**, *5*, 13475.
[9] E. Alonso, A. M. Sherman, T. J. Wallington, M. P. Everson, F. R. Field, R. Roth, R. E. Kirchain, *Environ. Sci. Technol.* **2012**, *46*, 3406.
[10] W. Xue, Y. Yang, Q. Yang, Y. Liu, L. Wang, C. Chen, R. Cheng, *RSC Adv.* **2018**, *8*, 13083.
[11] J. Li, Z. Liu, W. Ma, H. Dong, K. Zhang, R. Wang, *J. Power Sources* **2019**, *412*, 189.
[12] C. Cao, Z.-B. Li, X.-L. Wang, X.-B. Zhao, W.-Q. Han, *Front. Energy Res.* **2014**, *2*, 1.
[13] N. Imanishi, O. Yamamoto, *Mater. Today Adv.* **2019**, *4*, 100031.
[14] R. DeWees, H. Wang, *ChemSusChem* **2019**, *12*, 3713.
[15] D. Zhang, X. Xu, Q. Yanlin, S. Ji, Y. Huo, Z. Wang, Z. Liu, J. Shen, J. Liu, *Chem. A Eur. J.* **2020**, *26*, 1720.
[16] D. Zhang, X. Xu, X. Huang, Z. Shi, Z. Wang, Z. Liu, R. Hu, J. Liu, M. Zhu, *J. Mater. Chem. A* **2020**, *8*, 18043.
[17] J. Liu, T. Liu, Y. Pu, M. Guan, Z. Tang, F. Ding, Z. Xu, Y. Li, *RSC Adv.* **2017**, *7*, 46545.
[18] K. Kwatek, W. Ślubowska, J. Trébosc, O. Lafon, J. L. Nowiński, *J. Eur. Ceram. Soc.* **2020**, *40*, 85.
[19] A. Rosenberger, Y. Gao, L. Stanciu, *Solid State Ionics* **2015**, *278*, 217.
[20] C.-M. Chang, Y. Il Lee, S.-H. Hong, H.-M. Park, *J. Am. Ceram. Soc.* **2005**, *88*, 1803.
[21] C. Wang, W. Ping, Q. Bai, H. Cui, R. Hensleigh, R. Wang, A. H. Brozena, Z. Xu, J. Dai, Y. Pei, C. Zheng, G. Pastel, J. Gao, X. Wang, H. Wang, J.-C. Zhao, B. Yang, X. R. Zheng, J. Luo, Y. Mo, B. Dunn, L. Hu, *Science (80-.)* **2020**, *368*, 521.
[22] J. Gao, Y.-S. Zhao, S.-Q. Shi, H. Li, *Chinese Phys. B* **2016**, *25*, 018211.
[23] V. Siller, A. Morata, M. N. Eroles, R. Arenal, J. C. Gonzalez-Rosillo, J. M. López del Amo, A. Tarancón, *J. Mater. Chem. A* **2021**, *9*, 17760.
[24] C. Vinod Chandran, S. Pristat, E. Witt, F. Tietz, P. Heitjans, *J. Phys. Chem. C* **2016**, *120*, 8436.
[25] M. Monchak, T. Hupfer, A. Senyshyn, H. Boysen, D. Chernyshov, T. Hansen, K. G. Schell, E. C. Bucharsky, M. J. Hoffmann, H. Ehrenberg, *Inorg. Chem.* **2016**, *55*, 2941.
[26] I. McClelland, B. Johnston, P. J. Baker, M. Amores, E. J. Cussen, S. A. Corr, *Annu. Rev. Mater. Res.* **2020**, *50*, 371.
[27] P. Senguttuvan, G. Rousse, J. Oró-Solé, J. M. Tarascon, M. R. Palacín, *J. Mater. Chem. A* **2013**, *1*, 15284.
[28] K. Lasri, M. Dahbi, A. Liivat, D. Brandell, K. Edström, I. Saadoune, *J. Power Sources* **2013**, *229*, 265.
[29] Y. Fu, H. Ming, S. Zhao, J. Guo, M. Chen, Q. Zhou, J. Zheng, *Electrochim. Acta* **2015**, *185*, 211.
[30] M. Giarola, A. Sanson, F. Tietz, S. Pristat, E. Dashjav, D. Rettenwander, G. J. Redhammer, G. Mariotto, *J. Phys. Chem. C* **2017**, *121*, 3697.
[31] E. Dashjav, Q. Ma, Q. Xu, C.-L. Tsai, M. Giarola, G. Mariotto, F. Tietz, *Solid State Ionics* **2018**, *321*, 83.
[32] F. Single, B. Horstmann, A. Latz, *J. Phys. Chem. C* **2019**, *123*, 27327.
[33] T. E. Ashton, J. V. Laveda, D. A. MacLaren, P. J. Baker, A. Porch, M. O. Jones, S. A. Corr, *J. Mater. Chem. A* **2014**, *2*, 6238.
[34] R. S. Hayano, Y. J. Uemura, J. Imazato, N. Nishida, T. Yamazaki, R. Kubo, *Phys. Rev. B* **1979**, *20*, 850.
[35] T. E. Ashton, P. J. Baker, D. Bauer, A. R. Groves, C. Sotelo-Vazquez, T. Kamiyama, T. Matsukawa, K. M. Kojima, J. A. Darr, *J. Mater. Chem. A* **2020**, *8*, 11545.
[36] T. E. Ashton, P. J. Baker, C. Sotelo-Vazquez, C. J. M. Footer, K. M. Kojima, T. Matsukawa, T. Kamiyama, J. A. Darr, *J. Mater. Chem. A* **2021**, *9*, 10477.
[37] R. Borg, G. Dienes, in *An Introduction to Solid State Diffusion*, Elsevier, Burlington, MA **2012**.
[38] J. Rodríguez-Carvajal, *Phys. B Condens. Matter* **1993**, *192*, 55.
[39] K. Momma, F. Izumi, *J. Appl. Crystallogr.* **2011**, *44*, 1272.
[40] F. L. Pratt, *Phys. B Condens. Matter* **2000**, *289–290*, 710.
[41] M. Pérez-Estébanez, J. Isasi-Marín, D. M. Többens, A. Rivera-Calzada, C. León, *Solid State Ionics* **2014**, *266*, 1.
[42] E. C. Bucharsky, K. G. Schell, A. Hintennach, M. J. Hoffmann, *Solid State Ionics* **2015**, *274*, 77.
[43] L. Huang, Z. Wen, M. Wu, X. Wu, Y. Liu, X. Wang, *J. Power Sources* **2011**, *196*, 6943.
[44] K. Arbi, S. Mandal, J. M. Rojo, J. Sanz, *Chem. Mater.* **2002**, *14*, 1091.
[45] N. Kosova, E. Devyatkina, D. Osintsev, *J. Mater. Sci.* **2004**, *39*, 5031.